Sound & Vibration 2026, 60(5), 4458.
doi: https://doi.org/10.59400/sv4458

Article

Meta-lens for acoustic concentration and enhanced sensing via transformation acoustics

Botao Yang, Li Cai*, Kunsheng Xing, Shixin Yu, Huajie Hong

College of Intelligence Science and Technology, National University of Defense Technology, Changsha 410073, China
*** Corresponding author:** Li Cai, cailiyunnan@163.com

CITATION

Yang B, Cai L, Xing K, et al. Meta-lens for acoustic concentration and enhanced sensing via transformation acoustics. Sound & Vibration. 2026; 60(5): 4458. https://doi.org/10.59400/sv4458

ARTICLE INFO

Received: 29 May 2026
Revised: 30 June 2026
Accepted: 7 July 2026
Available online: 24 July 2026

Abstract: Detecting weak acoustic signals requires broadband energy concentration, but the acoustic power coupled into a device can be strongly curtailed by impedance mismatch at the inlet. Here, we develop a transformation-acoustics-based acoustic meta-lens in which a rectangular virtual domain is mapped to a trapezoidal physical domain, directing incident energy toward a narrow output aperture. In contrast to an air-filled trapezoidal horn with the same outer envelope, the meta-lens reshapes the wavefront through a spatially varying anisotropic mass-density tensor and an equivalent bulk modulus. A cubic-polynomial transition layer is introduced at the inlet to bridge the parameter jump between air and the anisotropic equivalent medium. Finite-element simulations from 200 to 3,000 Hz show positive sound transmission gain for the original design, with a mean value of 3.582 dB. With the transition layer, the mean gain increases to 5.470 dB, the minimum gain rises from 2.695 dB to 3.672 dB, and the mean inlet reflection coefficient decreases from 0.5644 to 0.3239, corresponding to a reduction of 42.6%. A genetic algorithm optimization of the lens length, inlet width, outlet width, and transition-layer thickness further increases the maximum gain from approximately 6.54 dB to 7.36 dB and the minimum gain from approximately 3.67 dB to 4.14 dB. These results indicate that inlet impedance grading and geometric optimization can work together to provide more robust broadband acoustic concentration for weak-signal sensing.

Keywords: transformation acoustics; acoustic energy concentration; broadband enhancement; impedance transition layer; genetic algorithm

1. Introduction

Acoustic-signal enhancement is a fundamental problem in acoustic sensing, information acquisition, and wave-field manipulation. Its objective is to improve the detectability, directivity, and spatial resolution of a target acoustic signal without substantially increasing the source power. This technology has been widely used in medical ultrasound imaging, underwater acoustic communication, industrial nondestructive testing, and environmental noise monitoring [1]. Conventional enhancement strategies mainly rely on increasing the excitation intensity or on back-end digital signal processing. Under complex propagation conditions, strong background noise, or weak-signal detection scenarios, however, these methods are often constrained simultaneously by energy consumption, signal-to-noise ratio, array aperture, and algorithmic robustness [2–4]. Therefore, directly tailoring the acoustic-energy distribution during propagation by means of artificial structures has become an important route for overcoming the bottlenecks of conventional acoustic enhancement. Among such structures, acoustic metamaterials (AMMs) and phononic crystals can reconstruct effective acoustic parameters at subwavelength scales and provide new physical degrees of freedom for acoustic-wave propagation, focusing, isolation, and enhancement [5].

The development of acoustic metamaterials has substantially expanded the boundaries of sound-field control [5–9]. These artificially engineered composites are typically composed of periodically or aperiodically arranged subwavelength unit cells and can exhibit effective parameters that are difficult to obtain in natural materials, such as negative mass density, negative bulk modulus, and strongly anisotropic responses [10]. Driven by different objectives in acoustic-field manipulation, several representative research directions have emerged in recent years. For example, in reflection and transmission control, phase-gradient acoustic metasurfaces can realize wavefront-shaping functionalities such as anomalous reflection, anomalous refraction, and beam splitting [11]. In nonreciprocal and direction-selective transmission, nonlinear effects and structural symmetry breaking have been used to construct acoustic diodes and asymmetric transmission devices [12]. In complex spatial sound-field reconstruction, acoustic holography can generate prescribed three-dimensional fields by controlling the phase and amplitude of two-dimensional acoustic pixels, showing potential for biomedical manipulation and imaging [13]. Meanwhile, studies on acoustic-energy concentration and local enhancement have continued to advance; gradient-index lenses, super-oscillatory lenses, and compact acoustic amplification structures have been used to increase local sound pressure and overcome conventional diffraction limitations [14,15].

Among these directions, acoustic-energy focusing and compression for sensing applications constitute an important topic. Unlike pure signal post-processing, physical-structure-based enhancement can redistribute acoustic energy before the waves reach the receiver, which increases the effective signal strength at the source of the detection chain. Chen et al. [16] reported pressure compression based on anisotropic acoustic metamaterials at an early stage, providing an important concept for using transformation media to concentrate acoustic energy. Subsequently, gradient-index structures were employed for acoustic focusing and weak-signal detection [15,17]. In local-resonance enhancement, coupled Helmholtz and Fabry-Perot resonance models have been used to improve voice acquisition [18], and space-coiling structures have also been adopted to enhance acoustic output in smart wearable devices [19]. In addition, phononic-crystal-coupled structures offer considerable design flexibility for signal enhancement, and related studies have demonstrated three-dimensional acoustic-field manipulation and broadband enhancement responses [20,21].

Despite substantial progress, acoustic-metamaterial-based enhancement devices still face two key challenges that affect practical applications. The first is limited operating bandwidth. Many high-gain structures rely on local resonances or multiple coupled resonances, so their enhancement is usually confined to a limited frequency range. To broaden the operating band, researchers have proposed dual-gradient structures, fractal rainbow trapping, and multiscale gradient designs [22,23]. However, these methods are often accompanied by increased structural complexity, higher parameter sensitivity, and greater fabrication difficulty. For broadband sensing, a device must not only achieve high gain at a single frequency but also maintain a stable and predictable enhancement response over a broad band. The second challenge arises from impedance mismatch. The effective parameters of metamaterials usually differ markedly from those of the background medium; when an acoustic wave impinges on the device interface, reflection and scattering can readily occur, reducing the effective acoustic energy coupled into the functional region. Previous studies have attempted to improve energy coupling using nonlocal coupling, impedance-matching layers, or gradient metamaterial interfaces [24,25]. Nevertheless, the simultaneous optimization of broadband operation, low reflection, and high gain while maintaining compactness remains challenging. In other words, the key to a broadband enhancement device is not merely to focus sound but also to efficiently couple incident acoustic energy into the device and stably compress it toward the output region during propagation.

Motivated by these considerations, this work develops a transformation-acoustics-based broadband enhancement acoustic meta-lens. The design maps a rectangular acoustic propagation region in virtual space onto a trapezoidal lens region in physical space, thereby inducing acoustic energy to converge progressively toward a narrow outlet along the propagation direction. To clarify the distinction between the role of transformation-acoustic equivalent parameters and that of a simple geometrical contraction, an air-filled trapezoidal horn with the same outer dimensions is used as a control structure, and the differences between the two structures are compared through their acoustic-field distributions. To reduce the abrupt inlet impedance transition between the homogeneous background medium and the anisotropic equivalent medium, a cubic-polynomial graded transition layer is further introduced at the input end, enabling the equivalent density tensor and bulk modulus to vary smoothly from the background-air parameters to the inlet parameters of the meta-lens. A genetic algorithm (GA) is then used to jointly optimize the lens length, inlet width, outlet width, and transition-layer thickness. Simulation results show that, after optimization, the maximum sound transmission gain over 200–3,000 Hz increases from approximately 6.54 dB to approximately 7.36 dB, while the minimum gain increases from approximately 3.67 dB to approximately 4.14 dB. These improvements indicate enhanced broadband performance and frequency response stability. Taken together, the results offer a feasible design route for enhancement devices intended for weak acoustic-signal detection and broadband acoustic sensing.

2. Design principle

The broadband enhancement acoustic meta-lens proposed in this work is based on transformation acoustics (TA). Originating from transformation optics, TA establishes a spatial mapping relationship through coordinate transformations and then derives the equivalent material parameters required for the desired acoustic-field control. It therefore provides a systematic framework for designing acoustic propagation paths, energy concentration, and impedance transitions [26].

TA constructs a coordinate mapping $x' = f(x)$ between virtual and physical spaces such that acoustic propagation in physical space is equivalent to acoustic propagation in virtual space. Accordingly, an originally simple acoustic propagation problem can be transformed into the design of spatially inhomogeneous and anisotropic acoustic material parameters in physical space.

Assume that the virtual space is a homogeneous isotropic acoustic medium with mass density ρ and bulk modulus κ. The physical-space coordinate is denoted by x', and the virtual-space coordinate by x; the two are related by the coordinate transformation $x' = f(x)$. The Jacobian matrix corresponding to this transformation is $J(x) = \partial x^{'} / \partial x$, with the specific form:

$$J(x, y, z) = \begin{bmatrix} \frac{\partial x^{'}}{\partial x} & \frac{\partial x^{'}}{\partial y} & \frac{\partial x^{'}}{\partial z} \\ \frac{\partial y^{'}}{\partial x} & \frac{\partial y^{'}}{\partial y} & \frac{\partial y^{'}}{\partial z} \\ \frac{\partial z^{'}}{\partial x} & \frac{\partial z^{'}}{\partial y} & \frac{\partial z^{'}}{\partial z} \end{bmatrix}, \tag{1}$$

whose determinant is denoted as det $(J(x))$.

To preserve the form of the acoustic governing equations in physical space relative to those in virtual space, the equivalent mass-density tensor $\widetilde{\rho}$ and equivalent bulk modulus $\widetilde{\kappa}$ in physical space must satisfy the following transformation relations [27]:

$$\widetilde{\rho}(x^{'}) = \rho|det(J(x))|(J^{-1}(x))^T J^{-1}(x), \tag{2}$$

$$\widetilde{\kappa}(x^{'}) = \kappa|det(J(x))|. \tag{3}$$

In this equivalent medium, the acoustic pressure p and particle velocity v are jointly determined by the anisotropic mass-density tensor and the bulk modulus.

Inspired by the wave-gathering effect of conventional acoustic horn structures [28] and motivated by the need for broadband acoustic-energy concentration, a TA-based acoustic meta-lens is developed in this study. As shown in **Figure 1**, the structure maps a rectangular virtual domain of length L and height w_1 onto a trapezoidal physical domain with the same length L, inlet width w_1, and outlet width w_2. This mapping effectively introduces nonuniform compression in the y direction that varies with x in virtual space, thereby inducing the acoustic wave to gradually converge toward the central axis during propagation.

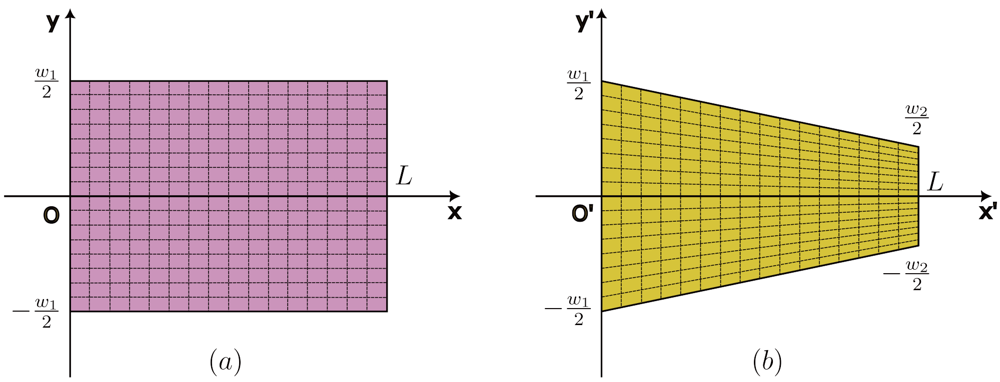

Figure 1. **(a)** Virtual space; **(b)** Physical space.

The coordinate transformation from virtual space to physical space for the acoustic lens is defined as:

$$x^{'} = x, \quad y^{'} = g(x)y, \quad z^{'} = z, \tag{4}$$

where $g(x)$ is the spatial compression factor and describes the degree of scale contraction in the *y* direction. For the linear compression mapping used in this study, $g(x)$ is expressed as:

$$g(x) = \frac{\frac{w_2 - w_1}{L}x + w_1}{w_1}. \tag{5}$$

From Equation (4), the corresponding Jacobian matrix is obtained as:

$$J(x, y) = \begin{bmatrix} 1 & 0 & 0 \\ g^{'}(x)y & g(x) & 0 \\ 0 & 0 & 1 \end{bmatrix}, \tag{6}$$

where $g^{'}(x)$ is the first derivative of the compression factor $g(x)$ with respect to x, namely:

$$g^{'}(x) = \frac{dg(x)}{dx} = \frac{w_2 - w_1}{Lw_1}. \tag{7}$$

According to Equations (2) and (3), the equivalent mass-density tensor and equivalent bulk modulus in the acoustic meta-lens can be written as:

$$\widetilde{\rho} = \rho_0 \begin{bmatrix} \rho_{xx} & \rho_{xy} & 0 \\ \rho_{yx} & \rho_{yy} & 0 \\ 0 & 0 & \rho_{zz} \end{bmatrix}, \tag{8}$$

$$\widetilde{\kappa} = \kappa_0 g(x), \tag{9}$$

where ρ_0 and κ_0 are the mass density and bulk modulus of the homogeneous background medium, respectively. The components of the equivalent mass-density tensor are:

$$\rho_{xx} = g(x) + \frac{(g^{'}(x)y)^2}{g(x)}, \tag{10}$$

$$\rho_{yy} = \frac{1}{g(x)}, \tag{11}$$

$$\rho_{zz} = g(x), \tag{12}$$

$$\rho_{xy} = \rho_{yx} = -\frac{g^{'}(x)y}{g(x)}. \tag{13}$$

These equivalent parameters indicate that the designed acoustic meta-lens is not a homogeneous medium but instead exhibits a spatially continuous and anisotropic acoustic response. The compression factor $g(x)$ controls the gradual variation of the material parameters along the lens length, so that the acoustic wave is continuously guided after entering the lens and is progressively concentrated toward the narrow outlet region during propagation. Unlike acoustic enhancement structures that rely on local resonances, the proposed design primarily uses coordinate-transformation-induced spatial compression to concentrate acoustic energy; hence, it can maintain a stable enhancement capability over a relatively broad frequency range.

To quantitatively characterize the signal-enhancement capability of the acoustic meta-lens, the sound transmission gain (STG) is adopted as the main evaluation metric [29]. To avoid the influence of reflected waves at the incident boundary on the normalization, the denominator of the STG is defined using the reference intensity of a prescribed incident plane wave in background air. The STG is defined as:

$$\mathrm{STG} = 10log_{10}\frac{\bar{I}_{\mathrm{out}}}{\bar{I}_{\mathrm{inc}}}, \tag{14}$$

where $\bar{I}_{\mathrm{out}}$ is the mean transmitted acoustic intensity at the output boundary, and $\bar{I}_{\mathrm{inc}}$ is the reference acoustic intensity of the prescribed incident plane wave in background air. The reference incident intensity is:

$$\bar{I}_{\mathrm{inc}} = \frac{|p_0|^2}{2\rho_0 c_0}, \tag{15}$$

where p_0 is the prescribed incident pressure amplitude. The mean transmitted acoustic intensity at the output boundary is obtained by integrating the normal component of the time-averaged acoustic intensity:

$$\bar{I}_{\mathrm{out}} = \frac{1}{L_{\mathrm{out}}}\int_{\Omega_{\mathrm{out}}}\frac{1}{2}\mathrm{Re}\left(p\mathbf{v}^*\right)\cdot\mathbf{n}_{\mathrm{out}}ds, \tag{16}$$

where L_{out} is the output-aperture width, p is the complex acoustic pressure, $\mathbf{v}^*$ is the complex conjugate of the particle velocity, $\mathbf{n}_{\mathrm{out}}$ is the outward unit normal vector of the output boundary, and ds is the differential line element. The STG defined in this manner directly reflects the enhancement of the output intensity relative to the prescribed incident wave while avoiding contamination of the normalization reference by the reflected wave at the inlet.

3. Modeling and simulation

To validate the acoustic-field manipulation capability of the designed broadband enhancement acoustic meta-lens, numerical modeling and frequency-domain simulations are conducted using the finite-element method in the Acoustics Module of COMSOL Multiphysics v.6.3. The simulations focus on the acoustic-field distribution, interfacial reflection, transmission gain, and broadband response stability to evaluate the effectiveness of the transformation-acoustic structure in broadband acoustic-energy concentration.

3.1. Original design

For the original structural model, the geometric parameters of the meta-lens are set as follows: inlet width w_1 = 2,000 mm, outlet width w_2 = 250 mm, and length L = 500 mm.

In the material and physics settings, the external background medium is homogeneous air with mass density ρ_0 = 1.225 kg/m^3, sound speed c_0 = 343 m/s, and bulk modulus $\kappa_0 = \rho_0 c_0^2 \approx$ 144.1 kPa. The meta-lens region is modeled as a spatially inhomogeneous and anisotropic equivalent fluid derived from transformation acoustics. In the "Pressure Acoustics, Frequency Domain" module of COMSOL, the anisotropic acoustics interface and anisotropic acoustic material node are used to define the equivalent mass-density tensor components ρ_{xx}, ρ_{vv}, ρ_{zz}, and ρ_{xv}, together with the equivalent bulk modulus $\widetilde{\kappa}$, as analytic functions of the spatial coordinates. The specific forms of these analytic functions are given in Equations (10)–(13), thereby accurately reproducing the acoustic properties of the meta-lens.

For the boundary conditions and excitation, acoustic waves are applied from the wide-aperture side and propagate toward the narrow-aperture side. The wave propagation is excited by adding a plane-wave radiation condition and prescribing an incident pressure field with an amplitude of 1 Pa. To emulate an unbounded domain and eliminate nonphysical reflections from the truncated outer boundaries, the computational domain is surrounded by perfectly matched layers, whose thickness is set to twice the maximum acoustic wavelength in the studied frequency band, i.e., $2\lambda_{max}$. For meshing and solver configuration, the two-dimensional computational domain is discretized using a physics-controlled free triangular mesh. To ensure sufficient spatial resolution throughout the broad frequency band, particularly for accurately resolving the rapidly varying anisotropic parameters inside the meta-lens, the maximum mesh-element size is limited to 1/6 of the wavelength corresponding to the highest simulated frequency.

The frequency-domain calculation is performed from 200 Hz to 3,000 Hz with a frequency step of 20 Hz, yielding responses at 141 discrete frequency points. The band of 200–3,000 Hz is selected for two main reasons. First, the acoustic wavelength in air at 200 Hz is approximately 1.72 m, which is much larger than the original lens length of 0.50 m; this represents a relatively low-frequency and subwavelength operating condition and allows the effectiveness and limitations of the structure for low-frequency acoustic-energy concentration to be examined. Second, the wavelength at 3,000 Hz is approximately 0.114 m, which allows the acoustic-field variations to be adequately resolved by the finite-element mesh while covering the low-to-mid-frequency range relevant to many broadband acoustic sensing and weak-signal acquisition scenarios. Consequently, this frequency band can simultaneously probe different operating regimes, including low-frequency size limitation, mid-frequency coupling, and higher-frequency wavefront guidance.

To distinguish the effect of the transformation-acoustic parameters from that of simple geometric contraction, an air-filled trapezoidal horn with the same geometric parameters is also analyzed as a control. This control structure retains w_1 = 2,000 mm, w_2 = 250 mm, and L = 500 mm, but the internal medium is no longer assigned the anisotropic equivalent parameters derived from transformation acoustics; instead, it is filled with homogeneous air identical to the background medium. The walls of the trapezoidal channel are set as sound-hard boundaries to emulate an air-filled trapezoidal horn constrained by rigid walls. **Figure 2** shows the acoustic-pressure distributions of the transformation-acoustic meta-lens at 1,000 Hz, 2,000 Hz, and 3,000 Hz, together with that of the horn at 2,000 Hz.

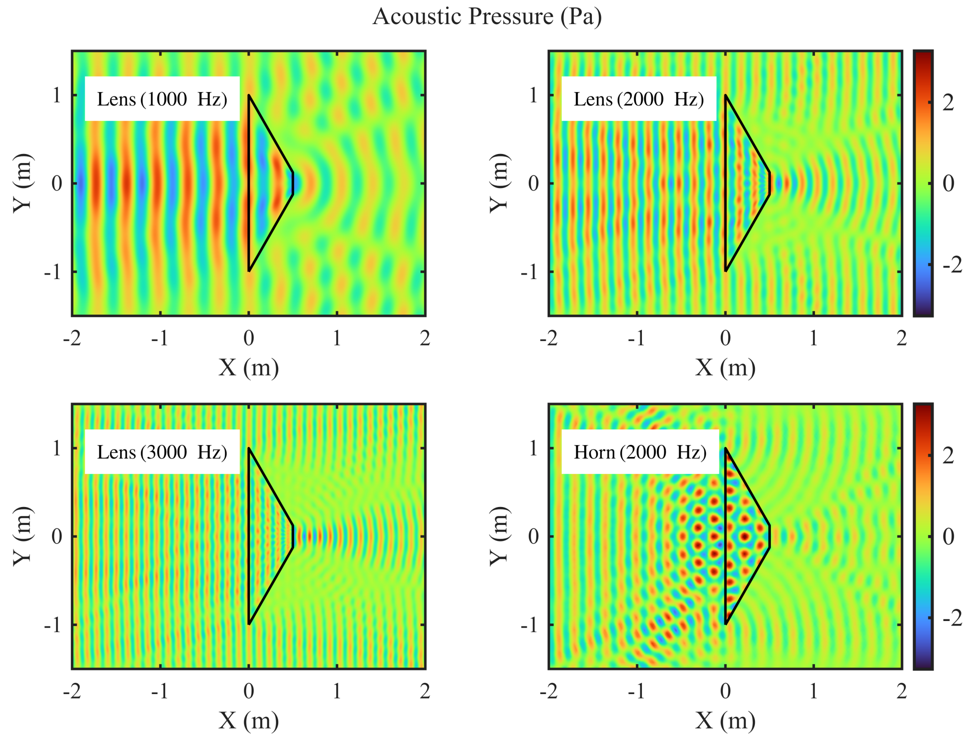

Figure 2. Acoustic pressure distributions of the acoustic meta-lens at 1,000 Hz, 2,000 Hz, and 3,000 Hz, together with the pressure field of an air-filled trapezoidal horn of identical outer dimensions at 2,000 Hz.

The simulations indicate that after the incident plane wave enters the acoustic meta-lens from the wide-aperture end, it gradually converges toward the central axis under the continuous modulation of the anisotropic equivalent medium, forming a pronounced sound-pressure enhancement region near the narrow output aperture. This behavior suggests that the transformation-acoustic structure can effectively guide acoustic-wave propagation and concentrate acoustic energy. In a conventional air-filled trapezoidal horn, the internal medium is homogeneous air, and the acoustic field is mainly governed by rigid-wall reflection, aperture diffraction, and wave interference. Although the geometric contraction of the horn can produce local pressure redistribution near the narrow outlet, the 2,000 Hz simulated field exhibits distinct interference fringes inside the channel rather than continuous and stable compression of the incident wavefront. Simulations at other frequencies also indicate that the horn response is highly frequency dependent. At most frequencies in the investigated band, the internal acoustic field is dominated by quasi-standing-wave interference patterns produced by the coupling between the wavelength and the rigid trapezoidal boundaries. Only within a relatively narrow frequency interval, when the internal phase relationship happens to favor constructive superposition near the outlet, can a certain focusing effect occur. Therefore, the enhancement of the proposed structure does not originate merely from the geometric narrowing of a horn but mainly from the continuous wavefront guidance and spatial compression provided by the transformation-acoustic parameters.

Similar focusing features are observed for the acoustic meta-lens at the three representative frequencies, indicating its basic potential for broadband operation. However, pronounced pressure fluctuations remain near the incident side, suggesting that the abrupt parameter change between homogeneous air and the anisotropic equivalent medium causes interfacial reflection and scattering. To further explain the inlet-interface effect, the normal impedance characteristics of the original meta-lens are analyzed using the transformation-acoustic equivalent-fluid model. For a plane wave normally incident on an anisotropic equivalent-fluid interface, the effective density involved in impedance matching is not a single tensor component but the projection of the equivalent density tensor along the interface-normal direction:

$$\rho_n = \left(\mathbf{n}^T \widetilde{\rho}^{-1} \mathbf{n}\right)^{-1}, \tag{17}$$

where **n** is the outward unit normal vector of the incident boundary. The corresponding normal effective sound speed and normal characteristic acoustic impedance are:

$$c_n = \sqrt{\frac{\widetilde{\kappa}}{\rho_n}}, \tag{18}$$

$$Z_n = \rho_n c_n = \sqrt{\rho_n \widetilde{\kappa}}. \tag{19}$$

For the geometry considered here, the acoustic wave propagates along the *x* direction. Therefore, the above expressions incorporate the influence of the anisotropic density tensor on normal propagation through $\widetilde{\rho}^{-1}$. The acoustic impedance of the background air is:

$$Z_0 = \rho_0 c_0 = \sqrt{\rho_0 \kappa_0}. \tag{20}$$

Because both the equivalent density tensor and the bulk modulus inside the meta-lens differ from those of homogeneous air, discontinuities in the effective acoustic parameters inevitably exist at the incident interface. These discontinuities cause part of the incident acoustic energy to be reflected and scattered at the inlet, leading to the nonideal pressure distribution near the incident side in **Figure 2**.

To quantitatively characterize inlet reflection, the reflection coefficient at the incident side is further extracted from the simulation results. The incident acoustic power is calculated from the prescribed incident plane-wave intensity on the inlet boundary:

$$P_{\text{inc}} = \bar{I}_{\text{inc}} L_{\text{in}}, \tag{21}$$

where L_{in} is the inlet-boundary width. The net acoustic power entering the computational domain is obtained by integrating the *x* component of the time-averaged acoustic intensity over the same boundary:

$$P_{\text{net}} = \int_{\Omega_{\text{in}}} \frac{1}{2} \text{Re}\left(p \mathbf{v}^*\right) \cdot \mathbf{e}_x ds. \tag{22}$$

The reflected acoustic power is calculated as:

$$P_{\text{ref}} = P_{\text{inc}} - P_{\text{net}}, \tag{23}$$

and the reflection coefficient is defined as:

$$R = \frac{P_{\text{ref}}}{P_{\text{inc}}}. \tag{24}$$

Table 1 lists the reflection coefficients of the original meta-lens at representative frequencies. The reflection coefficient increases from 0.2803 at 200 Hz to 0.5557 at 400 Hz and remains at a relatively high level over 600–3,000 Hz. The average reflection coefficient over the sampled band is approximately 0.5644. This result indicates that the original design suffers from significant reflection loss at the incident interface, mainly due to the abrupt parameter change between homogeneous air and the anisotropic equivalent medium.

Table 1. Simulated reflection coefficients of the original meta-lens at the incident boundary.

Frequency (Hz)	R(f)	Frequency (Hz)	R(f)
200	0.2803	1,800	0.5879
400	0.5557	2,000	0.5894
600	0.5800	2,200	0.5969
800	0.5720	2,400	0.5984
1,000	0.5790	2,600	0.5980
1,200	0.5691	2,800	0.5931
1,400	0.5778	3,000	0.5980
1,600	0.5904		

Figure 3 presents the STG of the original acoustic meta-lens at 141 frequency points from 200 Hz to 3,000 Hz. The STG remains positive throughout the investigated band, indicating that the original structure can realize broadband acoustic-energy concentration. The maximum gain is 4.222 dB at 200 Hz, the minimum gain is 2.695 dB at 480 Hz, and the average gain is 3.582 dB.

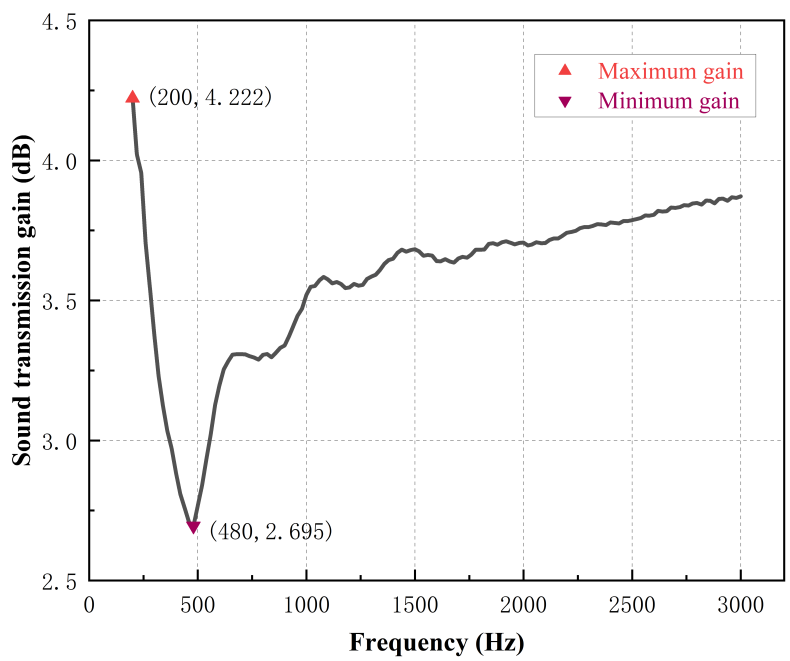

Figure 3. Transmission gain of the acoustic meta-lens from 200 Hz to 3,000 Hz.

In terms of frequency response, the STG of the meta-lens does not increase monotonically with frequency. Instead, it decreases rapidly from a high value and then gradually increases. As shown in **Table 1**, the reflection coefficient at 200 Hz is relatively low, allowing the incident acoustic energy to couple into the meta-lens structure more effectively and thus producing the maximum transmission gain of 4.222 dB. As the frequency increases to approximately 400–500 Hz, inlet reflection becomes significantly stronger, and unfavorable phase superposition and local standing-wave distributions are more readily formed inside the lens. Consequently, the STG decreases rapidly and reaches its minimum value of 2.695 dB at 480 Hz. Above 600 Hz, although inlet reflection remains relatively high, the acoustic wavelength gradually decreases relative to the device size, and the wavefront-guiding effect of the anisotropic equivalent medium becomes stronger. Acoustic energy is then reconcentrated toward the narrow output aperture, causing the STG to increase slowly and remain within approximately 3.3–3.9 dB in the mid-to-high-frequency range.

These results suggest that the main bottleneck of the meta-lens is not the absence of an acoustic-energy concentration mechanism but the abrupt interface between homogeneous air and the anisotropic equivalent medium, which weakens the incident coupling efficiency and induces gain fluctuations within the band. Therefore, introducing a graded transition layer at the input end to smooth the variation of the equivalent parameters and reduce interfacial reflection is necessary to further improve broadband transmission gain and response stability.

3.2. Introduction of the graded transition layer

To mitigate impedance mismatch caused by the boundary, a graded transition layer is introduced at the incident end of the acoustic meta-lens so that the acoustic parameters vary continuously between the background medium and the lens inlet instead of changing abruptly. The purpose of this design is not to alter the transformation-acoustic mapping of the meta-lens body but to provide a buffer region at the incident side, which improves the coupling of acoustic energy from homogeneous air into the anisotropic equivalent medium.

As shown in **Figure 4a**, the transition-layer thickness is denoted by T_{in}, and its spatial coordinates are denoted by (*x, y*). Along the *x* direction, the transition layer occupies the interval $[-T_{\text{in}}, 0]$; along the *y* direction, it covers $[-w_1/2, w_1/2]$. To ensure parameter continuity at the incident side, the transition layer must satisfy the boundary matching conditions at both the background-medium end and the meta-lens end:

- At the left boundary $x = -T_{\text{in}}$, the equivalent parameters of the transition layer are those of background air:

$$\widetilde{\rho}_{\text{trans}}(-T_{\text{in}}) = \rho_0 I, \widetilde{\kappa}_{\text{trans}}(-T_{\text{in}}) = \kappa_0;$$

- At the right boundary $x = 0$, the equivalent parameters of the transition layer match those at the inlet cross-section of the acoustic meta-lens:

$$\widetilde{\rho}_{\text{trans}}(0) = \rho_{\text{lens}},\ \widetilde{\kappa}_{\text{trans}}(0) = \kappa_{\text{lens}}.$$

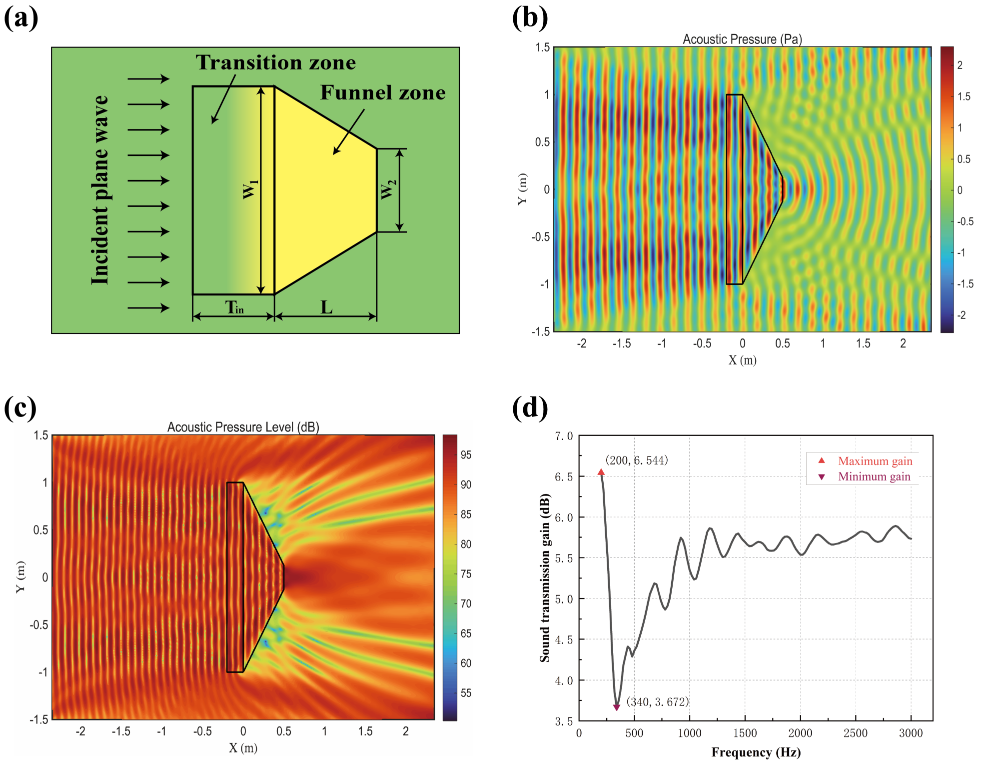

Figure 4. **(a)** Schematic of the acoustic meta-lens with an input transition layer; **(b)** Simulated acoustic-pressure field at 2,000 Hz; **(c)** Simulated sound-pressure-level field at 2,000 Hz; **(d)** Transmission gain of the transition-layer-assisted acoustic meta-lens at 141 frequency points over 200–3,000 Hz.

Within the transition layer, the equivalent mass-density tensor components P_{ij} (such as ρ_{xx}, ρ_{vv}, ρ_{zz}, and ρ_{xv}) and the equivalent bulk modulus κ are interpolated as follows:

$$P_{ij}(x', y') = P_{ij,b} + f(s) \cdot (P_{ij,f}(0, y') - P_{ij,b}), \tag{25}$$

$$\kappa(x', y') = \kappa_b + f(s) \cdot (\kappa_f(0, y') - \kappa_b), \tag{26}$$

where $s = (x + T_{\text{in}})/T_{\text{in}}$ is the normalized coordinate along the x direction, with a range of $[0, 1]$. Here, $P_{ij,b}$ and κ_b represent the density tensor components and bulk modulus of the homogeneous background medium, respectively, whereas $P_{ij,f}(0, y')$ and $\kappa_f(0, y')$ represent the corresponding equivalent parameters at the inlet cross-section of the meta-lens.

The interpolation function $f(s)$ determines the spatial variation of the acoustic parameters in the transition layer. Linear gradient or discrete stepwise matching layers often introduce slope discontinuities at interfaces or between layers, thereby producing residual scattering [30]. Here, a cubic polynomial is used as the transition function:

$$f(s) = 3s^2 - 2s^3. \tag{27}$$

This function satisfies $f(0) = 0$ and $f(1) = 1$, as well as $f'(0) = 0$ and $f'(1) = 0$. Therefore, the transition layer ensures not only continuity in the material-parameter values at both ends but also the absence of first-gradient discontinuities at the boundaries.

After a graded transition layer with thickness T_{in} = 200 mm is added at the incident end of the meta-lens, the acoustic field is recalculated. **Figure 4b,c** show the acoustic-pressure and sound-pressure-level distributions at 2,000 Hz for the structure with the transition layer. Compared with the case without the transition layer, the wavefront fluctuations near the incident end are reduced, and the spatial distribution of the acoustic field becomes smoother before entering the meta-lens body. This behavior indicates that the graded layer mitigates the abrupt coupling between homogeneous air and the anisotropic equivalent medium to some extent, allowing more acoustic energy to enter the compression-type meta-lens region rather than being reflected back into the background domain at the inlet.

To directly verify the suppression of inlet reflection by the graded transition layer, Equations (21)–(24) are used to calculate the reflection coefficients after adding the transition layer. **Table 2** presents the results at representative frequencies of 200–3,000 Hz. Compared with the original structure in **Table 1**, the inlet reflection coefficient decreases markedly at every frequency after the transition layer is introduced. The average reflection coefficient over the sampled band decreases from 0.5644 for the original structure to 0.3239, corresponding to an absolute reduction of 0.2405 and a relative reduction of approximately 42.6%. This behavior suggests that the cubic-polynomial graded transition layer not only increases the output sound transmission gain but also genuinely reduces the reflection loss caused by the abrupt inlet-parameter transition.

Table 2. Simulated reflection coefficients of the meta-lens with the graded transition layer at the incident boundary.

Frequency (Hz)	R(f)	Frequency (Hz)	R(f)
200	0.1555	1,800	0.3383
400	0.3052	2,000	0.3563
600	0.3232	2,200	0.3343
800	0.3373	2,400	0.3394
1,000	0.3321	2,600	0.3321
1,200	0.3965	2,800	0.3278
1,400	0.3101	3,000	0.3396
1,600	0.3314		

A point worth emphasizing is that the graded transition layer used here is not a quarter-wavelength matching layer designed for a single frequency; hence, its goal is not to achieve exact zero reflection at a particular frequency. For example, when T_{in} = 200 mm, the acoustic wavelength in air at 200 Hz is approximately 1.72 m, so the transition-layer thickness is approximately 0.12λ, which remains subwavelength. At 3,000 Hz, by contrast, the transition-layer thickness is approximately 1.75λ. Thus, the function of the transition layer is to smooth abrupt equivalent-parameter variations and reduce overall inlet reflection over a broad frequency band, rather than to act as a conventional single-frequency quarter-wavelength matching layer. The enhancement in the low-frequency range remains jointly limited by the overall device size, inlet coupling, and output-aperture diffraction.

Figure 4d shows the STG curve of the structure with the graded transition layer over 200–3,000 Hz. Compared with the original structure, the transition layer raises the overall gain level throughout the band and improves the response at low-gain frequencies. Specifically, after the transition layer is introduced, the average gain reaches 5.470 dB, the maximum gain is 6.544 dB, and the minimum gain increases from 2.695 dB for the original structure to 3.672 dB. Together with **Table 2**, this result shows that the gain improvement is consistent with the reduction in the inlet reflection coefficient, indicating that the graded transition layer converts the acoustic-energy concentration capability of the original transformation-acoustic structure into output transmission enhancement more effectively by improving the incident acoustic-energy coupling efficiency.

3.3. Optimization of geometric parameters

After the input graded transition layer based on the cubic interpolation function $f(s)$ is introduced, the impedance discontinuity between the background medium and the acoustic meta-lens is partly alleviated. However, the frequency-response curve still exhibits pronounced fluctuations in the sound transmission gain over the studied band. These fluctuations are mainly associated with residual interfacial reflection, diffraction at the output aperture, and phase superposition inside the tapered anisotropic medium. Therefore, improving inlet coupling using the transition layer alone is insufficient to fully exploit the broadband enhancement potential of the structure; the overall geometry of the meta-lens must also be further tuned.

We therefore use a GA to jointly optimize four key geometric parameters: the meta-lens length L, inlet aperture width w_1, outlet aperture width w_2, and input transition-layer thickness T_{in}. Specifically, L primarily affects phase accumulation and longitudinal standing-wave distributions inside the lens; w_1 determines the acoustic-energy capture area at the incident end; w_2 controls the spatial compression ratio and diffraction intensity near the output end; and T_{in} affects the smoothness of the impedance transition between air and the anisotropic equivalent medium. These parameters are not independent; instead, they collectively determine acoustic-energy coupling, transmission compression, and output radiation. Hence, they are optimized here as a set of coupled design variables.

The optimization is implemented through a coupled Python-COMSOL framework. For each candidate parameter set generated by the GA, the program first updates the geometric variables in the COMSOL model, then rebuilds the geometry, remeshes the model, performs the frequency-domain solution, and finally extracts the STG values at all sampled frequencies for fitness evaluation.

For a candidate design, the STG at the sampled frequencies is denoted by G_i, where $i = 1, 2, \ldots, N$ and N is the number of frequency samples. The average gain, minimum gain, maximum gain, and standard deviation are defined as:

$$G_{\text{avg}} = \frac{1}{N} \sum_{i=1}^{N} G_i, \tag{28}$$

$$G_{\text{min}} = \min_{1 \le i \le N} G_i, \tag{29}$$

$$G_{\text{max}} = \max_{1 \le i \le N} G_i, \tag{30}$$

$$G_{\text{std}} = \sqrt{\frac{1}{N} \sum_{i=1}^{N} \left(G_i - G_{\text{avg}}\right)^2}. \tag{31}$$

The meta-lens with the input transition layer but without geometric optimization is used as the reference structure. The corresponding performance metrics are denoted by $G_{\text{avg}}^{\text{ref}}$, $G_{\text{min}}^{\text{ref}}$, $G_{\text{max}}^{\text{ref}}$, and $G_{\text{std}}^{\text{ref}}$. During the optimization, these reference values are obtained from simulations of the baseline model with the input transition layer but without geometric optimization. To avoid imbalanced contributions from different objective terms due to differences in dimension and numerical scale, a normalized gain scale S is introduced:

$$S = \max\left(G_{\text{max}}^{\text{ref}} - G_{\text{min}}^{\text{ref}}, 1\text{dB}\right). \tag{32}$$

The normalized average-gain term, minimum-gain term, and spectral-fluctuation term are defined as:

$$\Phi_{\text{avg}} = \frac{G_{\text{avg}} - G_{\text{avg}}^{\text{ref}}}{S}, \tag{33}$$

$$\Phi_{\text{min}} = \frac{G_{\text{min}} - G_{\text{min}}^{\text{ref}}}{S}, \tag{34}$$

$$\Phi_{\text{std}} = \frac{G_{\text{std}}}{S}. \tag{35}$$

To prevent the optimization from increasing the average gain at the expense of the worst-frequency performance, an additional penalty term is introduced when the minimum gain of a candidate structure is lower than that of the reference structure:

$$\Phi_{\text{pen}} = \left[\frac{max\left(0, G_{\text{min}}^{\text{ref}} - G_{\text{min}}\right)}{S}\right]^2. \tag{36}$$

The final normalized fitness function is expressed as:

$$F = w_{\text{avg}}\Phi_{\text{avg}} + w_{\text{min}}\Phi_{\text{min}} - w_{\text{std}}\Phi_{\text{std}} - \beta\Phi_{\text{pen}}, \tag{37}$$

where w_{avg}, w_{min}, and w_{std} are the weighting coefficients for the average gain, minimum gain, and in-band fluctuation terms, respectively, and β is the penalty coefficient. In this work, w_{avg} = 0.45, w_{min} = 0.35, w_{std} = 0.20, and β = 2.0. This fitness function enables the optimization process to account simultaneously for the broadband average gain, worst-frequency response, and spectral flatness, thereby avoiding geometries that perform well only at localized frequencies.

The optimization ranges of the geometric parameters are listed in **Table 3**. The parameter bounds consider the baseline structure size, device compactness, acoustic compression strength, and numerical stability of the finite-element calculations. An excessively short L may lead to overly abrupt parameter variations, whereas an excessively long L weakens device compactness. A smaller w_2 can enhance the compression effect but may also intensify output diffraction and increase the degree of anisotropy in the effective parameters. The value of T_{in} must balance impedance-transition smoothness and overall device size.

Table 3. Optimization ranges of geometric parameters.

Parameter	Baseline value	Optimization range (m)
L	0.50 m	[0.36, 0.73]
w_1	2.00 m	[1.80, 2.20]
w_2	0.25 m	[0.18, 0.32]
T_{in}	0.20 m	[0.20, 0.50]

The GA uses a population size of 24 and a maximum of 40 generations. The crossover probability is 0.85, the mutation probability is 0.08, the mutation step size is 0.08 times the corresponding parameter range, the elite count is 2, and the tournament selection size is 3. In addition to the baseline reference simulation, the GA evaluates 984 candidate structures.

Figure 5a shows the variation of the fitness value during GA optimization. The fitness changes rapidly in the early stage, indicating that the algorithm quickly identifies high-performance parameter combinations from the initial random population. The curve then gradually enters a plateau, suggesting that the population has converged toward a relatively stable design region. The local fluctuations during optimization mainly arise from crossover and mutation operations; these perturbations help maintain population diversity and reduce the probability of becoming trapped in a local optimum.

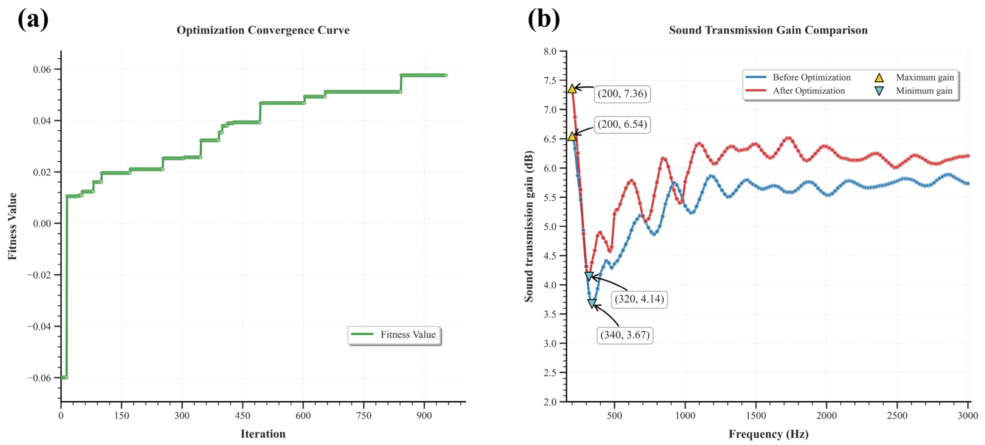

Figure 5. **(a)** Fitness-value curve during GA optimization; **(b)** Comparison of sound transmission gain before and after GA optimization.

After the GA search, the preferred geometric parameter combination is found to be $L = 0.54$ m, $w_1 = 2.19$ m, $w_2 = 0.18$ m, and $T_{in} = 0.22$ m. Compared with the baseline structure, this parameter set keeps the overall device size under control while increasing the inlet acoustic-energy capture capability, strengthening the geometric compression effect, and further optimizing the input impedance transition.

Figure 5b compares the sound transmission gain curves before and after optimization. Before optimization, the maximum STG is approximately 6.54 dB and the minimum STG is approximately 3.67 dB. After GA optimization, the maximum STG increases to approximately 7.36 dB and the minimum STG increases to approximately 4.14 dB. This behavior indicates that the optimized geometry not only enhances acoustic-energy concentration in favorable frequency ranges but also raises the response at low-gain frequencies, which improves broadband operating stability.

The performance improvement originates from the coordinated effects of multiple geometric factors. By adjusting L, the optimization algorithm modifies the phase accumulation process inside the lens and weakens unfavorable standing-wave conditions. By tuning w_1 and w_2, the structure achieves a more appropriate balance among incident acoustic-energy capture, spatial compression strength, and output-end diffraction. Meanwhile, optimizing T_{in} further improves the impedance transition at the inlet. Thus, the GA does not simply search for the extremum of a single parameter; instead, it identifies a combination of multiple coupled geometric variables that jointly improves broadband transmission behavior.

4. Results and discussion

This section discusses the broadband enhancement performance of the acoustic meta-lens and its underlying physical mechanisms. Three aspects are analyzed: first, the difference in acoustic-energy concentration between the transformation-acoustic meta-lens and the air-filled trapezoidal horn; second, the improvement in interfacial reflection and broadband transmission stability provided by the input graded transition layer; and third, the influence of coordinated geometric parameter tuning on the enhancement of sound transmission gain, based on the GA optimization results.

4.1. Role of transformation-acoustic parameters in acoustic energy concentration

The original acoustic meta-lens exhibits positive sound transmission gain throughout 200–3,000 Hz, indicating that the transformation-acoustics-based spatial compression structure can concentrate acoustic energy effectively over a broad frequency band. Without the transition layer, the maximum STG is 4.222 dB at 200 Hz, the minimum STG is 2.695 dB at 480 Hz, and the average gain is 3.582 dB. These results suggest that even without inlet impedance matching, the transformation-acoustic parameters provide clear physical support for acoustic-energy compression.

Compared with an air-filled trapezoidal horn of the same geometric dimensions, the advantage of the proposed structure does not arise solely from geometric convergence caused by the reduced outlet aperture. The medium inside the horn is still air, and acoustic propagation is mainly governed by boundary reflection, aperture diffraction, and scattering caused by geometric discontinuities. As a result, pronounced interference fringes readily appear in its acoustic field, and the energy distribution depends more strongly on local boundary conditions. By contrast, the transformation-acoustic meta-lens continuously modulates the propagation direction of the wavefront through spatially varying equivalent density tensors and bulk modulus, causing the acoustic wave to converge progressively toward the central axis and the narrow outlet region after entering the lens. Therefore, the enhancement mechanism is closer to wavefront reconstruction driven by equivalent medium parameters than to a simple geometric throat contraction.

The frequency response of the original structure shows a pronounced trough in the low-frequency region, particularly near 480 Hz. This behavior is associated with inlet impedance discontinuity and internal phase superposition. **Table 1** shows that, except at 200 Hz, the reflection coefficient at the incident boundary generally remains high, at approximately 0.56–0.60. Strong inlet reflection reduces the effective acoustic energy entering the functional region and induces standing-wave-like fluctuations in some frequency ranges. Therefore, although the original structure already possesses broadband enhancement capability, its performance is still limited by the inlet coupling efficiency.

4.2. Effect of the graded transition layer

Instead of judging the impedance-matching effect solely from the smoothing of the acoustic field, this work further quantifies the role of the transition layer through the reflected power at the inlet. The original structure has an average reflection coefficient of 0.5644 over the sampled 200–3,000 Hz band, whereas this value decreases to 0.3239 after the graded transition layer is introduced. Except near 1,200 Hz, where the reflection remains relatively high, the reflection coefficients at the other frequencies are generally maintained around 0.31–0.36, clearly below the approximately 0.56–0.60 level of the original structure. This result directly demonstrates that the transition layer not only changes the local acoustic-field morphology but also effectively improves the coupling efficiency of incident acoustic energy into the transformation-acoustic functional region.

The input graded transition layer substantially improves the coupling process as the acoustic wave enters the anisotropic equivalent medium from homogeneous air. Through a cubic-polynomial interpolation function, the transition layer makes the equivalent density tensor and bulk modulus vary continuously from the background-medium parameters to the meta-lens inlet parameters, preventing an abrupt parameter jump at the interface. Compared with linear transitions or stepped matching structures, the cubic polynomial ensures continuity of both the parameter values and their first derivatives at the two boundaries, thereby more effectively reducing residual scattering induced by gradient discontinuities.

The acoustic-field distribution shows that, after adding the transition layer, wavefront fluctuations near the input end are weakened, and the field near the lens inlet becomes smoother. This behavior indicates that the graded layer acts as a buffer between the background medium and the transformation-acoustic region, enabling more incident acoustic energy to enter the meta-lens body. Correspondingly, the sound transmission gain curve shifts upward overall. Before geometric optimization, the structure with the transition layer has a maximum STG of approximately 6.54 dB and a minimum STG of approximately 3.67 dB, representing a clear improvement relative to the original structure without the transition layer.

This result indicates that the principal loss in the original structure does not arise from the acoustic-energy compression mechanism itself but from the impedance discontinuity at the input end. The graded transition layer does not change the coordinate mapping of the meta-lens body, but it significantly improves the coupling efficiency of incident acoustic energy into the functional region. Therefore, for this type of transformation-acoustics-based broadband enhancement device, the inlet matching layer is not merely an auxiliary component but a critical part that determines whether the broadband performance can be fully realized.

4.3. Mechanism of geometric parameter optimization

After the graded transition layer is introduced, the broadband response of the structure still exhibits certain frequency fluctuations, indicating that improving inlet coupling alone cannot completely eliminate internal phase interference and output diffraction effects. To further enhance broadband performance, a GA is used to jointly optimize L, w_1, w_2, and T_{in}. The preferred parameter set obtained by the optimization is L = 0.54 m, w_1 = 2.19 m, w_2 = 0.18 m, and T_{in} = 0.22 m, which reflects a trade-off among acoustic-energy capture, spatial compression, and impedance transition.

After optimization, the maximum STG increases from approximately 6.54 dB to approximately 7.36 dB, and the minimum STG increases from approximately 3.67 dB to approximately 4.14 dB. This behavior indicates that the GA does not merely raise the local peak gain; it also elevates the low-gain regions within the frequency band, thereby making the overall response more stable. For broadband acoustic sensing, this is particularly important because practical detection systems require reliable enhancement across the entire operating band rather than an extreme response at a single frequency.

Physically, adjusting L changes the propagation phase and standing-wave distribution inside the lens, helping to weaken destructive interference at unfavorable frequencies. Increasing w_1 improves the acoustic-energy capture capability at the incident end. Decreasing w_2 strengthens the spatial compression ratio but may also increase output diffraction; therefore, it must be balanced with the other parameters. Optimizing T_{in} further improves the input impedance transition. These results suggest that broadband enhancement performance is not determined by any single geometric parameter but is jointly controlled by inlet coupling, internal compression, and outlet radiation.

4.4. Limitations and future work

A point worth emphasizing is that the model used in this study is still based on the assumption of an ideal equivalent medium. In practical fabrication, accurately realizing a spatially continuous anisotropic density tensor with off-diagonal terms remains challenging. In addition, the present simulations do not fully account for viscous loss, thermal-conduction loss, material discretization errors, or fabrication tolerances. These factors may cause the gain of an experimental prototype to be lower than that predicted by ideal simulations.

Future work can proceed in three directions. First, discrete unit-cell structures, labyrinthine channels, or porous composite structures will be explored to approximate the required equivalent-parameter distributions and to assess the influence of parameter discretization on broadband gain. Second, thermoviscous loss models and fabrication-tolerance analyses will be incorporated to obtain performance predictions closer to experimental conditions. Finally, prototype fabrication and experimental validation will be conducted by coupling the proposed meta-lens with practical sensor receivers, so as to evaluate its performance in weak acoustic-signal sensing and broadband acoustic acquisition.

5. Conclusion

This study developed a broadband acoustic meta-lens based on transformation acoustics to concentrate incident acoustic energy toward a narrow output aperture. By mapping a rectangular virtual domain onto a trapezoidal physical domain, the proposed meta-lens achieves progressive wavefront compression through spatially varying anisotropic equivalent parameters. Compared with an air-filled trapezoidal horn of identical outer dimensions, the meta-lens provides more continuous wavefront guidance and more stable acoustic-energy concentration over the investigated frequency range.

Finite-element simulations over 200–3,000 Hz showed that the original meta-lens maintained a positive sound transmission gain, with an average value of 3.582 dB. Introducing a cubic-polynomial graded transition layer increased the average gain to 5.470 dB, raised the minimum gain from 2.695 dB to 3.672 dB, and reduced the average inlet reflection coefficient from 0.5644 to 0.3239, corresponding to a relative reduction of approximately 42.6%. After genetic-algorithm optimization of the lens length, inlet width, outlet width, and transition-layer thickness, the maximum gain increased from approximately 6.54 dB to 7.36 dB, while the minimum gain increased from approximately 3.67 dB to 4.14 dB. These results demonstrate that graded inlet matching and coordinated geometric optimization can jointly improve broadband acoustic-energy concentration and transmission stability, providing a feasible design strategy for weak acoustic-signal sensing.

Author contributions: Conceptualization, BY and LC; methodology, BY; software, BY; validation, BY, KX and SY; formal analysis, HH; investigation, BY; resources, LC; data curation, BY; writing—original draft preparation, BY; writing—review and editing, BY and LC; visualization, BY; supervision, LC; project administration, BY; funding acquisition, LC. All authors have read and agreed to the published version of the manuscript.

Funding: This research was funded by the National Natural Science Foundation of China, grant number 52475144.

Institutional review board statement: Not applicable. This study did not involve humans or animals.

Informed consent statement: Not applicable. This study did not involve human participants.

Data availability statement: The data supporting the findings of this study are available from the corresponding author upon reasonable request.

Conflict of interest: The authors declare no conflict of interest.

AI use statement: During the preparation of this manuscript, the authors used DeepSeek solely for language refinement. No AI tools were used for data analysis, interpretation, or generation of scientific content. All outputs were critically reviewed and edited by the authors. The authors take full responsibility for the integrity and accuracy of the work.

References

1. Benesty J, Cohen I, Chen J. Fundamentals of Signal Enhancement and Array Signal Processing, 1st ed. Wiley; 2018. doi: 10.1002/9781119293132
2. Doclo S, Kellermann W, Makino S, et al. Multichannel Signal Enhancement Algorithms for Assisted Listening Devices: Exploiting spatial diversity using multiple microphones. IEEE Signal Processing Magazine. 2015; 32(2): 18–30. doi: 10.1109/MSP.2014.2366780
3. Gannot S, Burshtein D, Weinstein E. Signal enhancement using beamforming and nonstationarity with applications to speech. IEEE Transactions on Signal Processing. 2001; 49(8): 1614–1626. doi: 10.1109/78.934132
4. Vary P, Martin R. Digital Speech Transmission and Enhancement, 1st ed. Wiley; 2024. doi: 10.1002/9781119060970
5. Cummer SA, Christensen J, Alù A. Controlling sound with acoustic metamaterials. Nature Reviews Materials. 2016; 1(3): 16001. doi: 10.1038/natrevmats.2016.1
6. Fok L, Ambati M, Zhang X. Acoustic Metamaterials. MRS Bulletin. 2008; 33(10): 931–934. doi: 10.1557/mrs2008.202
7. Ma G, Sheng P. Acoustic metamaterials: From local resonances to broad horizons. Science Advances. 2016; 2(2): e1501595. doi: 10.1126/sciadv.1501595
8. Guenneau S, Movchan A, Pétursson G, et al. Acoustic metamaterials for sound focusing and confinement. New Journal of Physics. 2007; 9(11): 399–399. doi: 10.1088/1367-2630/9/11/399
9. Lu MH, Feng L, Chen YF. Phononic crystals and acoustic metamaterials. Materials Today. 2009; 12(12): 34–42. doi: 10.1016/S1369-7021(09)70315-3
10. Liu Z, Zhang X, Mao Y, et al. Locally Resonant Sonic Materials. Science. 2000; 289(5485): 1734–1736. doi: 10.1126/science.289.5485.1734
11. Tian Y, Ge H, Lu MH, et al. Research advances in acoustic metamaterials. Acta Physica Sinica. 2019; 68(19): 194301. doi: 10.7498/aps.68.20190850
12. Yu Q, Zhang X, Zhao C, et al. Design of Fano resonance-like acoustic metamaterials for low-frequency acoustic isolation. Acta Materiae Compositae Sinica. 2024; 41(5): 2731–2741. Available online: https://fhclxb.buaa.edu.cn/en/article/doi/10.13801/j.cnki.fhclxb.20240827.004 (in Chinese)
13. Xu M, Harley WS, Ma Z, et al. Sound-Speed Modifying Acoustic Metasurfaces for Acoustic Holography. Advanced Materials. 2023; 35(14): 2208002. doi: 10.1002/adma.202208002
14. Li HH, Zheng B, Duan MS, et al. Helmholtz-Structured Two-Dimensional Super-Diffraction Meta-Lens. Frontiers in Physics. 2022; 10: 923637. doi: 10.3389/fphy.2022.923637
15. Wang X, Li J, Yang J, et al. Compact acoustic amplifiers based on non-adiabatic compression of sound in metamaterial waveguides. Applied Acoustics. 2023; 204: 109246. doi: 10.1016/j.apacoust.2023.109246
16. Chen Y, Liu H, Reilly M, et al. Enhanced acoustic sensing through wave compression and pressure amplification in anisotropic metamaterials. Nature Communications. 2014; 5(1): 5247. doi: 10.1038/ncomms6247
17. Chen T, Yu D, Wu B, et al. Weak Signals Detection by Acoustic Metamaterials-Based Sensor. IEEE Sensors Journal. 2021; 21(15): 16815–16825. doi: 10.1109/JSEN.2021.3076860
18. Cai X, Wang C, Huang Z, et al. Improved voice acquisition using acoustic metamaterials. Applied Physics Letters. 2023; 123(3): 031701. doi: 10.1063/5.0151962
19. Chen T, Wang C, Yu D. Pressure amplification and directional acoustic sensing based on a gradient metamaterial coupled with space-coiling structure. Mechanical Systems and Signal Processing. 2022; 181: 109499. doi: 10.1016/j.ymssp.2022.109499
20. Zhao X, Hao G, Shang Y, et al. Three-Dimensional Gradient Metamaterial Devices Coupled with Phononic Crystals for Acoustic Enhancement Sensing. Crystals. 2023; 13(8): 1191. doi: 10.3390/cryst13081191
21. Zhang S, Hao G, Zhao X, et al. Broadband acoustic signal enhancement via gradient metamaterials coupled to crystals. Frontiers in Physics. 2023; 11: 1240468. doi: 10.3389/fphy.2023.1240468
22. Ma F, Wang L, Zhang H, et al. A dual-gradient underwater meta-auricle for broadband sound signal enhancement. Applied Acoustics. 2023; 208: 109374. doi: 10.1016/j.apacoust.2023.109374

23. Davies B, Chaplain GJ, Starkey TA, et al. Graded Quasiperiodic Metamaterials Perform Fractal Rainbow Trapping. Physical Review Letters. 2023; 131(17): 177001. doi: 10.1103/PhysRevLett.131.177001
24. Popa BI. Broadband sound pressure enhancement in passive metafluids. Physical Review B. 2017; 96(9): 094305. doi: 10.1103/PhysRevB.96.094305
25. Wang Z, Lu X, Zhao Y, et al. Harnessing nonlocal coupling effect to enhance broadband sound insulation in gradient acoustic metamaterial. Extreme Mechanics Letters. 2025; 78: 102376. doi: 10.1016/j.eml.2025.102376
26. Cummer SA, Popa BI, Schurig D, et al. Scattering Theory Derivation of a 3D Acoustic Cloaking Shell. Physical Review Letters. 2008; 100(2): 024301. doi: 10.1103/PhysRevLett.100.024301
27. Cummer SA, Rahm M, Schurig D. Material parameters and vector scaling in transformation acoustics. New Journal of Physics. 2008; 10(11): 115025. doi: 10.1088/1367-2630/10/11/115025
28. Dix GR. Development and Comparison of Highly Directional Loudspeakers [Master's Thesis]. Brigham Young University; 2006. Available online: https://scholarsarchive.byu.edu/cgi/viewcontent.cgi?referer=&httpsredir=1&article=1877&context=etd
29. Shaikh S, Huang Y, Alharbi A, et al. Acoustic Propagation and Transmission Loss Analysis in Shallow Water of Northern Arabian Sea. Journal of Marine Science and Engineering. 2024; 12(12): 2256. doi: 10.3390/jmse12122256
30. Ji H, Qi A, Yang F, et al. Design of acoustic impedance gradient matching layers. Applied Acoustics. 2023; 211: 109549. doi: 10.1016/j.apacoust.2023.109549